Check for updates

Received: 29 October 2021 | Revised: 1 February 2022 | Accepted: 16 February 2022

DOI: 10.1002/cnm.3585

APPLIED RESEARCH

WILEY

Biomechanical response of human rib cage to cardiopulmonary resuscitation maneuvers: Effects of the compression location

Mario Suazo[1,3] | **Joan Herrero**[2] | **Gerard Fortuny**[1] | **Dolors Puigjaner**[1] | **Josep M. López**[1]

[1]Departament d' Enginyeria Informàtica i Matemàtiques, Universitat Rovira i Virgili, Tarragona, Catalunya, Spain

[2]Departament d' Enginyeria Química, Universitat Rovira i Virgili, Tarragona, Catalunya, Spain

[3]Departamento de Matemática Aplicada, Escuela de Matemática y Ciencias de la Computación, UNAH–VS, Tegucigalpa, Honduras

Correspondence
Josep M. López, Departament d' Enginyeria Informàtica i Matemàtiques, Universitat Rovira i Virgili, Av Països Catalans 26, Tarragona, Catalunya, Spain.
Email: josep.m.lopez@urv.cat

Funding information
Universitat Rovira i Virgili, Grant/Award Number: 2018PFR-URV-B2-29

Abstract

The biomechanical response of a human rib cage to cardiopulmonary resuscitation maneuvers was investigated by means of finite element simulations. We analyzed the effect of the location where the force was applied on the achieved compression depths and stress levels experienced by the breastbone and ribs. For compression locations on the breastbone, a caudal shift of the application area toward the breastbone tip resulted in a 17% reduction of the force required to achieve a target 5 cm compression depth. We found that the use of compression regions located on the costal cartilages would involve higher risk of rib fractures.

KEYWORDS

biomechanical response, cardiopulmonary resuscitation, compression point, finite element simulation, thoracic compressions

1 | INTRODUCTION

Cardiac arrest (CA) is one of the leading health problems that is responsible for a substantial number of deaths in industrialized countries.[1,2] The survival chances of patients suffering CA rely on the application of cardiopulmonary resuscitation (CPR) maneuvers in the first few minutes.[3] CPR maneuvers, first described in the early 1960s, are mainly based on thoracic compressions.[4] The quality of CPR is highly related to an adequate chest compression depth. A study based on a large sample of patients[5] found that higher survival rates were associated to a compression depth between 4.03 and 5.53 cm, with a survival peak at 4.56 cm. Notwithstanding, the latest CPR guidelines[6] still recommend a compression depth between 5 and 6 cm for an average adult. Hands position is another key factor in the effectiveness of CPR. Regarding this issue, CPR guidelines are not very specific, and they merely recommend that compression be performed on the lower half of the breastbone. Medical teams specialized in the resuscitation of critical patients perform personalized hemodynamic–directed CPR maneuvers with complex protocols[7–9] that take into account several parameters such as the compression depth and the compression point location, among others.

This is an open access article under the terms of the Creative Commons Attribution-NonCommercial-NoDerivs License, which permits use and distribution in any medium, provided the original work is properly cited, the use is non-commercial and no modifications or adaptations are made.
© 2022 The Authors. *International Journal for Numerical Methods in Biomedical Engineering* published by John Wiley & Sons Ltd.

A direct compression of the heart ventricles during CPR is convenient as it generates systemic and pulmonary circulation.[10] Papadimitriou et al.[11] concluded that the region between the 4th and the 6th rib was a convenient position for hand placement during chest compression as they found, analyzing CT images from patients, that right and left ventricles were in almost 100% of the cases located below that region. In contrast, compression of the large blood vessels, and in particular of the left ventricle outflow tract, has been associated with adverse effects on the efficacy of CPR and with a decrease of survival rates.[12,13] It seems well established that only a small proportion of the ventricle is subjected to external chest compression when CPR is performed according to the current guidelines.[12,14,15] Consequently, a caudal shifting of the compression location from the internipple line into the sternoxiphoid junction has been suggested.[16] Moreover, some recent experimental studies strongly suggest that shifting the compression location to the left of the breastbone centerline, in such a way that compression affects the left ventricle, may improve cardiac output during CPR.[17,18]

On a broader perspective, the injury risk associated to chest compressions should also be taken into account when trying to improve CPR technique. Even though skeletal chest injuries produced by CPR are quite common,[19] most of them are categorized as insignificant. However, some thoracic lesions are reported to have potentially fatal consequences.[20–22] Actually, when thoracic lesions secondary to CPR are sufficiently serious, they cause a deterioration of the elastic properties of the thorax. Retaining the capacity of the breastbone to regain its position during the thoracic decompression phase is a key aspect for maintaining the venous return.[23]

Finite element (FE) simulations can provide an alternative to CPR studies performed in human corpses, which are known to be very challenging.[24] Previous FE studies of the rib cage responses to compression were mostly focused on the simulation of car crash conditions (see, e.g., References 25–28). In the present study, we use FE to simulate the response to CPR maneuvers of an adult skeletal chest. Our main purpose is to investigate the effect of the compression location on the biomechanical response of the rib cage. In particular, we consider five different locations and we analyze output quantities that are good indicators of CPR performance and rib fracture risk,[29] namely the displacement experienced by the rib cage and the maximum level of rib stress. For each compression location, we also examine the dependence of the output quantities on the magnitude of the compression force applied.

2 | MODELS AND METHODS

Figure 1 shows the geometry model of the rib cage used in the current study. The model comprises the breastbone, the seven pairs of costal cartilages attached to it, 10 pairs of osseous ribs and nine sections of intercostal muscles (ICM), each one connected to a pair of contiguous ribs. The current rib cage model was based on computerized tomography

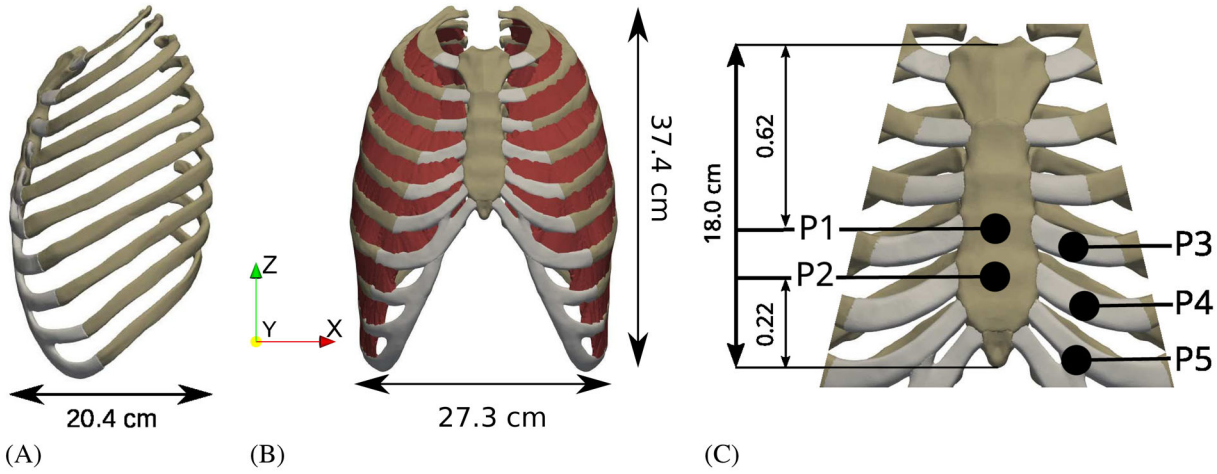

FIGURE 1 Geometry model used in the present study. (A) Sagittal view of the rib cage. (B) Anterior view, showing also the nine pairs of intercostal muscle sections in between ribs. (C) Magnification of part (B). Cartilaginous, osseous, and muscular tissue are respectively colored with light-gray, brown, and red. The solid circles in part (C) denote the approximate location of each of the five compression areas considered in the present simulations. The locations of the centers of the P1 and P2 compression areas, expressed as a percent of the length of the breastbone, are also included in this plot. Chest perimeter at P2 level is about 75 cm

(CT) images available in the BodyParts3D database for anatomy.[30] The CT images in this database were reconstructed from a complete set of magnetic resonance (MR) axial images, taken every 2 mm from the top of the head to the feet, of a 22–years–old volunteer whose body mass index was 21.7. During the acquisition of these images the subject was in a supine position with his hands on the sides of the body and his feet and ankles positioned as if the subject was standing.[31] Three dimensional (3D) triangular surface meshes for each of the individual elements in the model were first downloaded from the BodyParts3D database. Each of these individual surface meshes was subsequently refined and the ensemble of refined meshes was made physically consistent by removing undesirable intersections between contiguous elements. The consistent surface meshes, with a total of 1,235,972 triangles, were uploaded into the Gmsh software[32] where the corresponding 3D volume meshes were built. Finally all of the generated volume meshes were compounded into a global computational mesh consisting of 1,006,571 nodes and 4,388,675 tetrahedra. Numerical simulations were performed using the Code Aster open source FE software.[33]

The inset in part (C) of Figure 1 indicates the location of the five compression regions investigated. In the computational model, each compression region is characterized as a surface patch having an area of about 10 cm^2. These patches were devised to be representative of the average shape of the hypothenar eminence of the hand, which has been reported as the dominant area of force transmission during a manual chest compression.[34] The P1 and P2 compression regions are centered on the midline of the breastbone whereas the other three, P3, P4, and P5, are slightly shifted to the left and respectively centered on the cartilaginous tissue of the 4th, 5th and 6th left ribs. The center of the P1 (P2) area is located at a distance from the upper (lower) part of the breastbone equal to 62% (22%) of the breastbone length.

The costal cartilage was modeled as a homogeneous material with a linear isotropic elastic behavior. Costal cartilage usually undergoes a progressive calcification with age[35,36] and it is well established that the elastic modulus of the cartilage (E_c) is strongly dependent on its degree of calcification.[37,38] McCormick[35] developed a qualitative calcification score (CS) for costal cartilages based on an ordinal scale ranging between 0 (no calcification) and 4 (very severe calcification), with increments of 0.5. On the basis of extensive experimental data, Forman[37] proposed a mathematical relation between the cartilage apparent elastic modulus and McCormick's CS. In the present study, we assumed for all of the cartilages a CS of 1.5, which leads to $E_c = 27$ MPa according to Forman's formula. A value of the Poisson ratio of $\eta_c = 0.45$ was used in all the cartilages.

To validate the present model for the costal cartilages, we carried out numerical simulations of the experiments performed by Forman and Kent[39] (see Figure 2). The force–displacement curves shown in Figure 2C for different values of CS clearly indicate, as expected, a strong dependence of the cartilage stiffness (characterized by the slope of the force–displacement curves) on the tissue calcification level. Figure 2C also allows a qualitative comparison between the results produced by our model and the measurements and simulations previously reported by Forman and Kent[39] for their $415 - 4L$ specimen. In their mathematical model, Forman and Kent[39] implemented the linear isotropic elastic model for the bulk cartilaginous tissue together with a hyper-elastic non–isotropic constitutive model for the perichondrium. The perichondrium is the cartilage outermost layer, about one millimeter thick on the average and made of a fibrous tissue. It is well established that the contribution of the perichondrium to the overall cartilage stiffness is by no means negligible.[41] Nonetheless, both the model and the experimental test results of Forman and Kent[39] in Figure 2C show that the mechanical behavior of the cartilage as a whole is fairly well captured by the linear model, most commonly assumed in numerical simulations of the ribcage.

The breastbone and the osseous part of the ribs feature a complex structure in which an extremely hard external layer, the cortical bone, surrounds a much softer inner volume containing trabecular bone and marrow. From data reported in the literature,[42,43] it can be clearly inferred that there is a large inter–subject variation of the rib cortical bone material properties. For example, values of E ranging from 7 to 24 GPa were recently reported by Katzenberger et al.[43] from measurements with a sample of 58 subjects. Moreover, mechanical properties of bone tissues are known to be anisotropic. Some recent works[44–46] show that a map of the bone anisotropic directions can be systematically evaluated from CT scans, provided that the image resolution is high enough (few tens of a μm). However, micro–CT scans of an adult ribcage, which can only be obtained post–mortem because of the high-radiation levels involved, cannot currently achieve such high-resolution requirement. For example, image resolutions of at most some 80 μm were obtained in pediatric post–mortem micro–CT scans.[47] Thus, in the absence of a mapping of the osseous tissue organization, we opted for a simplified model, which can nonetheless characterize reasonably well the mean mechanical response of the ribs and breastbone. We modeled bone as a homogeneous material obeying an elasto–plastic von Mises behavior with linear isotropic hardening. In order to prescribe proper values of the constants in the bone constitutive model, we carried out FE simulations of Kindig et al.'s experiments[48] of rib bending under quasistatic frontal loading (see Figure 3A). These preliminary simulations, one for each osseous rib, were also used to test our model for the connections between

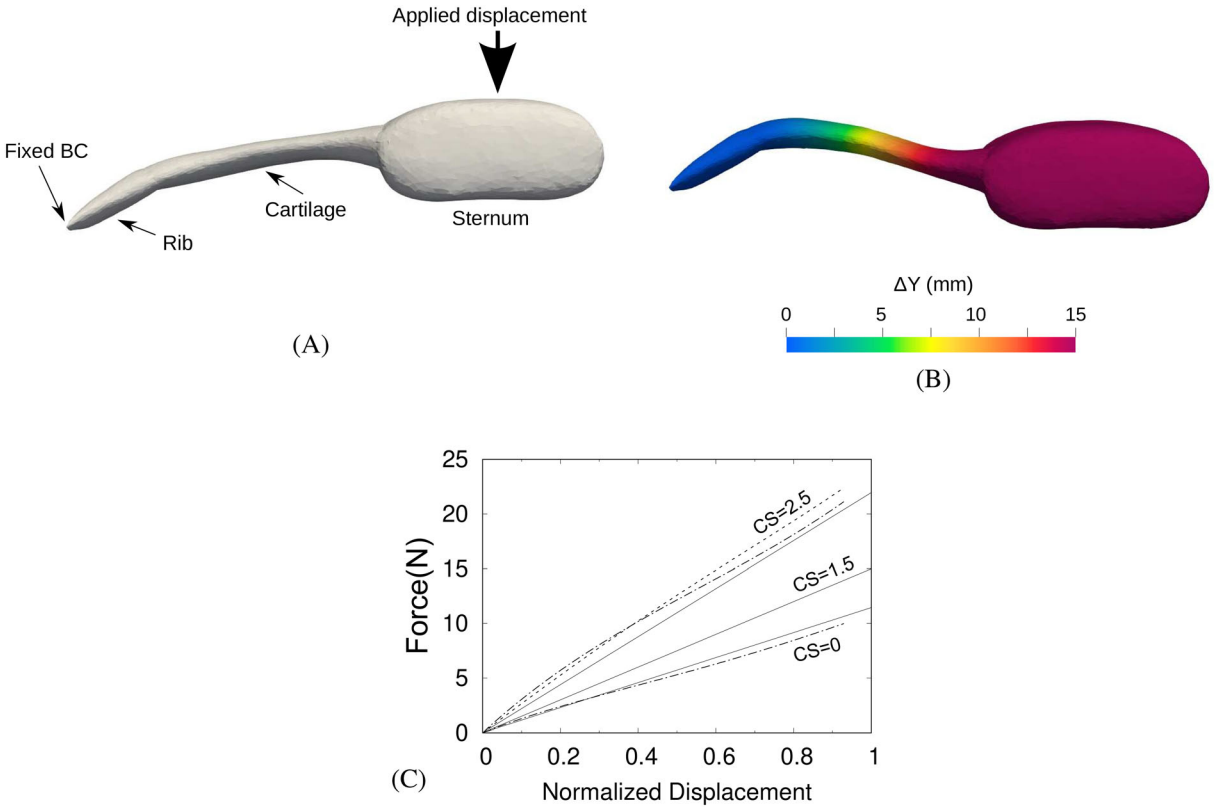

FIGURE 2 Comparison of our model with the experiments and simulations carried out by Forman et al.[39] for their 415 − 4L specimen. In their experimental setup,[40] sketched in part (A), one costal cartilage was attached to a section of the breastbone and to a small piece of the corresponding (osseous) rib. The breastbone was subjected to a vertical displacement (ΔY) and the reaction force exerted by the support was measured. The 4th left cartilage in the present geometry model was used in these simulations, with a maximum compression depth of $\Delta Y_{max} = 15$ mm (a value comparable with the maximum displacements applied in the experiments[39]). Since the outermost edge of the rib piece was fixed in the experiments a zero–displacement boundary condition (BC) was applied in the simulations. Part (B) shows the deformed geometry, with its surface colored according to the local displacement level, for the present model simulation with $E_c = 27$ MPa (CS = 1.5). Part (C) shows the reaction force (vertical component) as a function of the normalized applied diplacement ($\Delta Y/\Delta Y_{max}$) for three values of the calcification score, namely CS = 0 ($E_c = 21$ MPa), 1.5 ($E_c = 27$ MPa) and 2.5 ($E_c = 40$ MPa). Simulations with the present model are denoted by a solid line (——); measurements (CS = 2.5) and simulations (CS = 0, 2.5) reported by Forman and Kent[39] are respectively denoted by a dash (- - - -) and a dash–dot (-·-·-) line pattern

ribs and vertebrae. Our rib cage model assumes the spine to be fixed. As shown by Kindig et al.,[25] it is nonetheless important to allow some degree of rotation of the ribs relative to the costovertebral joints. In the present model, the desired rotation effect was achieved, as illustrated in Figure 3A, by inserting the posterior tip of the rib into a volume region of a softer tissue, which could be roughly understood to play the role of a joint capsule. The capsule material was assumed to behave as an elastic solid with a Young modulus of $E_j = 1$ MPa and a Poisson ratio of $\eta_j = 0.45$. Fixed (zero deformation) boundary conditions were prescribed only in a small patch located, in the context of Figure 3A, at the leftmost bottom region of the capsule surface. For every value of the applied force, F, the resulting deformation was recorded and the distribution of the von Mises tension, σ_v, was calculated. The highest levels of σ_v were found in the lateral region of the rib, as illustrated in Figure 3B for the case of the 5th left rib.

After extensive trial and error with the individual rib bending FE simulations, the chosen values for the characteristic parameters of the elasto–plastic bone model were: $E_b = 7$ GPa, $\sigma_Y = 30$ MPa (tensile yield strength), $E_T = 2$ GPa (tangent modulus) and $\eta_b = 0.4$. Figure 3C–E shows the force–deformation curves predicted using these parameter values in the cases of the 4th, 5th and 6th left ribs, that is, the ones that might be more affected in the FE simulations of the full rib cage when the compression force is applied in the P3, P4, or P5 regions (see Figure 1C). Basically, the value of E_b sets the initial slope in these curves. It is observed from the experimental curves that when the loading force reached a

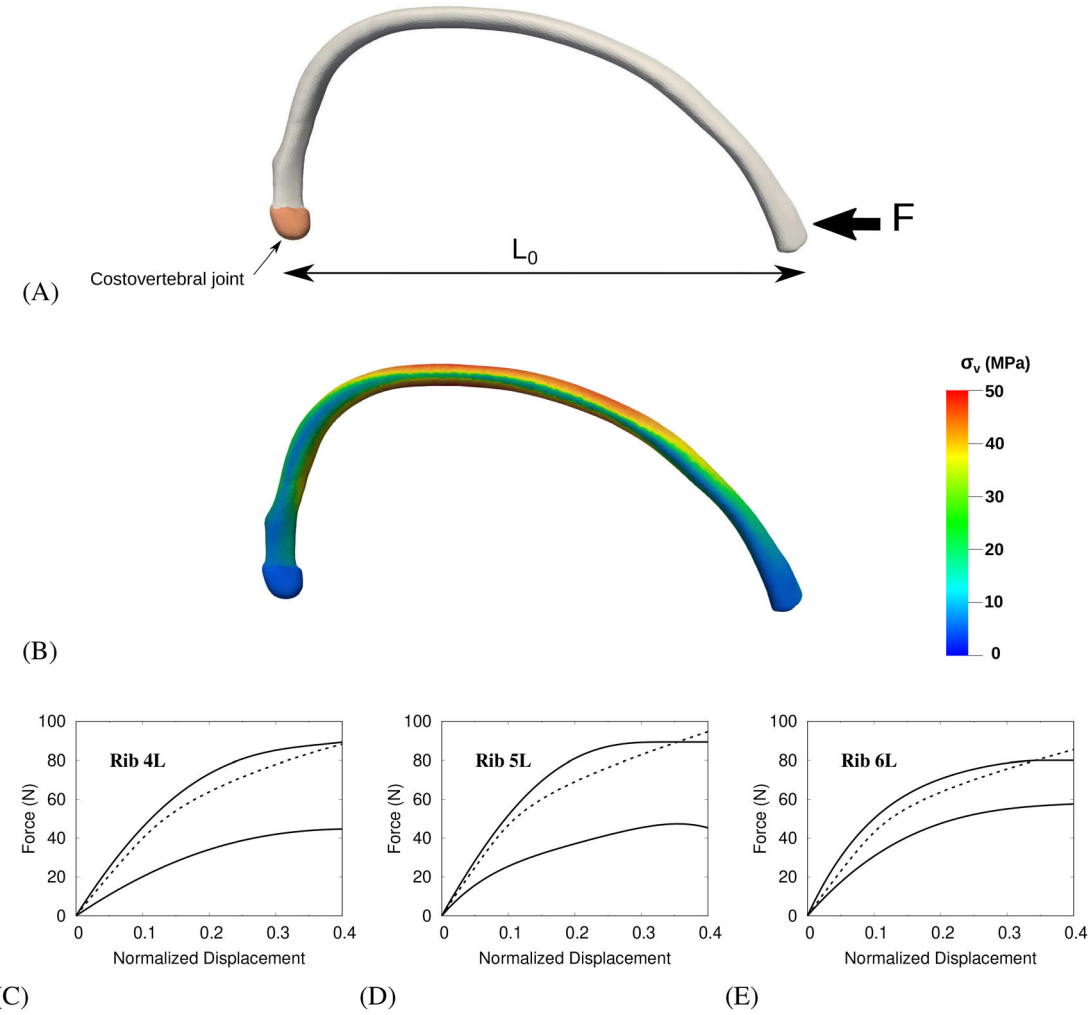

FIGURE 3 Examples of the current FE simulations of the rib bending experiments previously reported by Kindig et al.[48] (A) Geometric model for the osseous part of the 5th left rib (L5) and sketch of the boundary conditions applied. (B) Calculated von Mises stress distribution (σ_v) on the L5 surface when a force of $F = 60$ N is applied. (C–E) Predicted relative deformation ($1 - L/L_0$) as a function of F for the simulations of the 4th, 5th and 6th left ribs (dashed line); the respective extremal measurements, as reported by Kindig et al.,[48] are denoted in each plot by solid lines. FE, finite element

certain value, roughly within the 30 N $\leq F \leq$ 80 N range, the slope of the curve clearly undergoes a fast decay. In other words, beyond a certain level of the applied stress, σ_Y, the material appears to become increasingly softer.

In the elasto–plastic constitutive model, σ_Y denotes the stress level beyond which the material not just softens but it deteriorates, that is, it deforms irreversibly and is therefore indicative of the risk of fracture. Our rib model can more closely reproduce the flattening of the experimental curves at high-F values in Figure 3C–E if a sufficiently low-E_T value is used. However, in such a case the subsequent FE simulations of the whole rib cage would yield too large deformations when compression forces as high as $F = 600$ N are applied. We therefore opted for a more conservative approach with the rib cage model having a relatively high stiffness. Consequently, when analyzing the results of the FE simulations the risk of bone fractures will be associated with exceedingly high levels of the calculated stresses. Figure 3C–E, suggests that the irreversible plastic behavior typically dominates for applied forces larger than about $F = 60$ N. As seen in Figure 3B, for such a loading level the predicted distribution of von Mises tension in a rib peaks slightly above 50 MPa. We will therefore use in what follows the $\sigma_v = 50$ MPa reference level to qualitatively assess the risk of bone fractures in the FE simulations of the whole rib cage. In this respect, it is worth noting that Katzenberger et al.[43] reported values of the yield stress (σ_Y) in the 20–130 MPa range for the cortical rib bone whereas the corresponding range for the failure stress (σ_F) was 30–190 MPa.

Kindig et al.[25] also assessed the effect of the ICM on chest stiffness. In the present study, the ICM tissue has been charactertized as a linear isotropic elastic solid with a Young modulus of $E_m = 2$ MPa and a Poisson ratio of $\eta_m = 0.49$. The selected E_m value is higher than the one prescribed by Kindig et al.[25] for their base case ($E_m = 1.03$ MPa). Our choice for a higher E_m, considering as well that in our computational model the maximum thickness of each ICM section is in the 3–4 mm range, responds to our established bias, discussed above, toward a relatively stiff rib cage model. Kent[49] measured and classified chest stiffness in three categories, depending on the state of the specimen analyzed: intact, denuded, and eviscerated. Our rib cage model behaves, from a mechanical point of view, more as a denuded chest than as an eviscerated one.[49,50] That is, the extra stiffness provided to our rib cage model by the choice of the E_b, E_T, and E_m values partly compensates for the absence of internal tissues and viscera, which will obviously be present in a real patient subject to CPR.

We assumed that the patient was in supine position, which implies that parts of our rib cage model would be in contact with a (hypothetical) flat floor (or table) surface. In the model reference, (undeformed) geometry the 6th and 7th ribs would be the ones nearest to the floor level. We modeled a hypothetical rib–floor contact using a padding approach. Small cushion–like, originally straight, mesh volumes were adapted along its inner boundary to the posterior–most parts of ribs 7–10 whereas their outer flat boundaries were fixed at the floor level. The padding material was modeled as relatively hard elastic solid, with a Young modulus of $E_p = 10$ MPa and a Poisson ration of $\eta_p = 0.45$.

3 | RESULTS

Nine values for the compression force, ranging between $F = 200$ and 600 N in increments of 50 N, were applied to each of the five compression locations. This range of forces is consistent with the results reported by Beesems et al.,[51] who

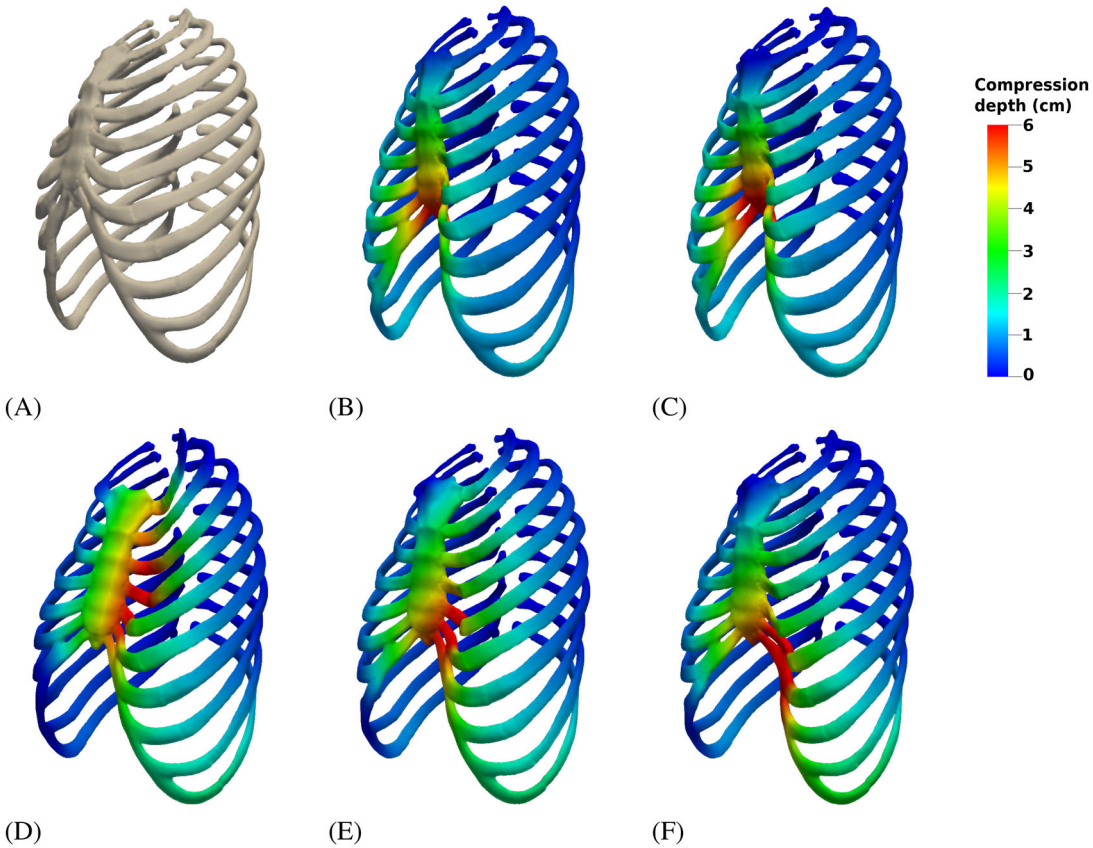

FIGURE 4 Predicted deformations experienced by the whole rib cage with 600 N compression force. (A) Original rib cage. (B–F) Deformed rib cage obtained when a compression was applied at the compression region: (B) P1, (C) P2, (D) P3, (E) P4, and (F) P5. The deformed rib cages are colored using the predicted distributions of the compression depth

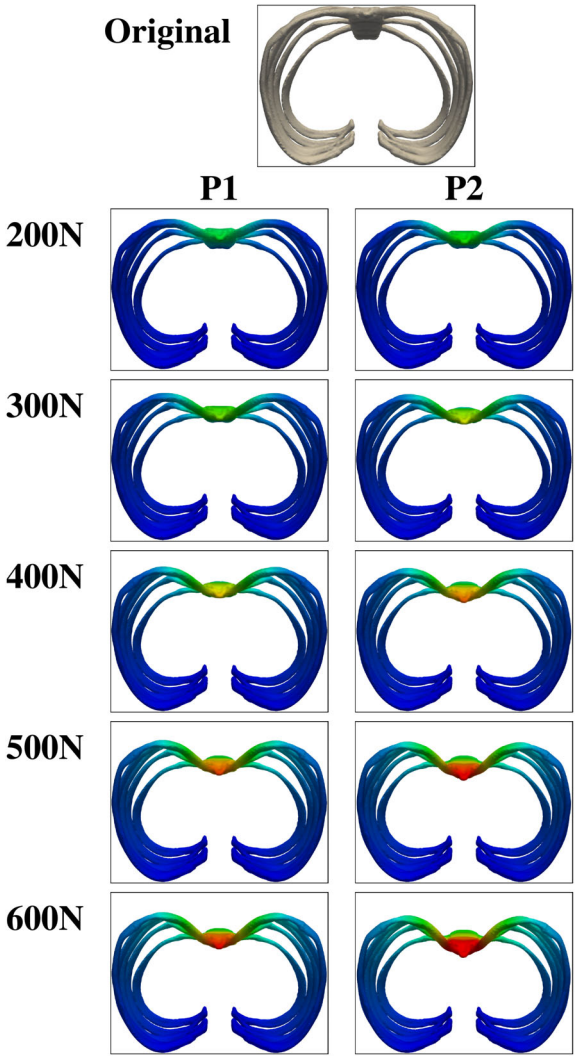

FIGURE 5 Caudal view of the region between 3rd and 7th ribs. Top figure corresponds to the original geometry (no force applied). Left and right columns correspond to deformed geometries obtained when a compression force, varying from 200 to 600 N (top to bottom), was applied over the P1 and P2 regions, respectively. Colors have the same meaning as in Figure 4

analyzed the CPR experimental data recorded in a chest compression device which had been set to a target compression depth of 5.3 ± 0.2 cm.

Figure 4 shows the predicted deformations experienced by the whole rib cage in the simulations with $F = 600$. For the sake of comparison, the undeformed rib cage is also included in part (A) of this figure. When the compression region is located on the breastbone (P1 and P2 cases), the rib cage deformation is almost bilaterally symmetric and the most deformed elements are the breastbone along with the 6th and 7th costal cartilages. Highly asymmetric patterns are instead obtained in the P3, P4 and P5 simulations (Figure 4D–F) where the element that undergoes the largest deformation is the costal cartilage at which the compression region is placed. Note that as the 6th and 7th cartilages are directly connected through cartilaginous tissue when one of these cartilages suffers a significant deformation the other one is also affected. A comparison between the results for P1 and P2 in Figure 4 reveals that the rib cage deformation is larger for the caudally shifted location P2 than it is for P1. The sequential caudal views of the deformed geometries displayed in Figure 5 reveal that the different behavior of P1 and P2 is observed for all levels of the applied force. Figure 5 also shows that as the breastbone moves inwards, the costal cartilages bend thus yielding a V–shaped form of the rib cage in which cartilages reach rather high angulations.

Figure 6 provides a quantitative assessment of the relationship between compression depth and force. This figure shows that, with the only exception of the P1 region, the maximum compression depths in a compression area are reached when compression is actually performed on it. Contrary to expectations, the maximum compression depths in

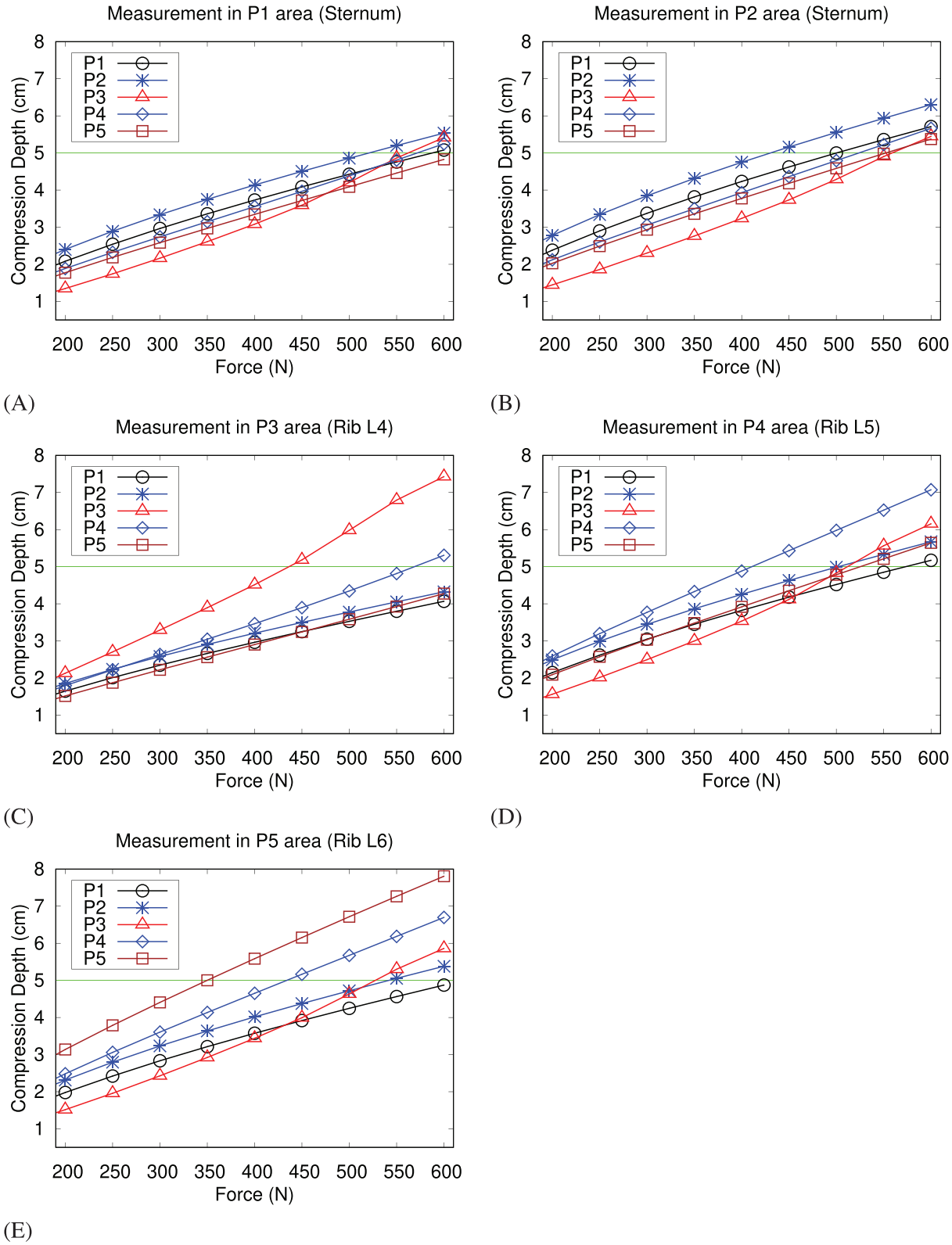

FIGURE 6 Maximum compression depth attained in the compression area (A) P1, (B) P2, (C) P3, (D) P4, and (E) P5 as a function of the amplitude of the force applied during the CPR maneuver over each of the five compression locations. CPR, cardiopulmonary resuscitation

the P1 area are reached when compression is performed on the P2 region (Figure 6A). Moreover, comparison of part (A) and (B) in Figure 6 reveals that, regardless of which of the five compression locations is used, less force is required to reach a certain compression depth in the breastbone P2 area than to achieve the same depth in the P1 area. It is thus

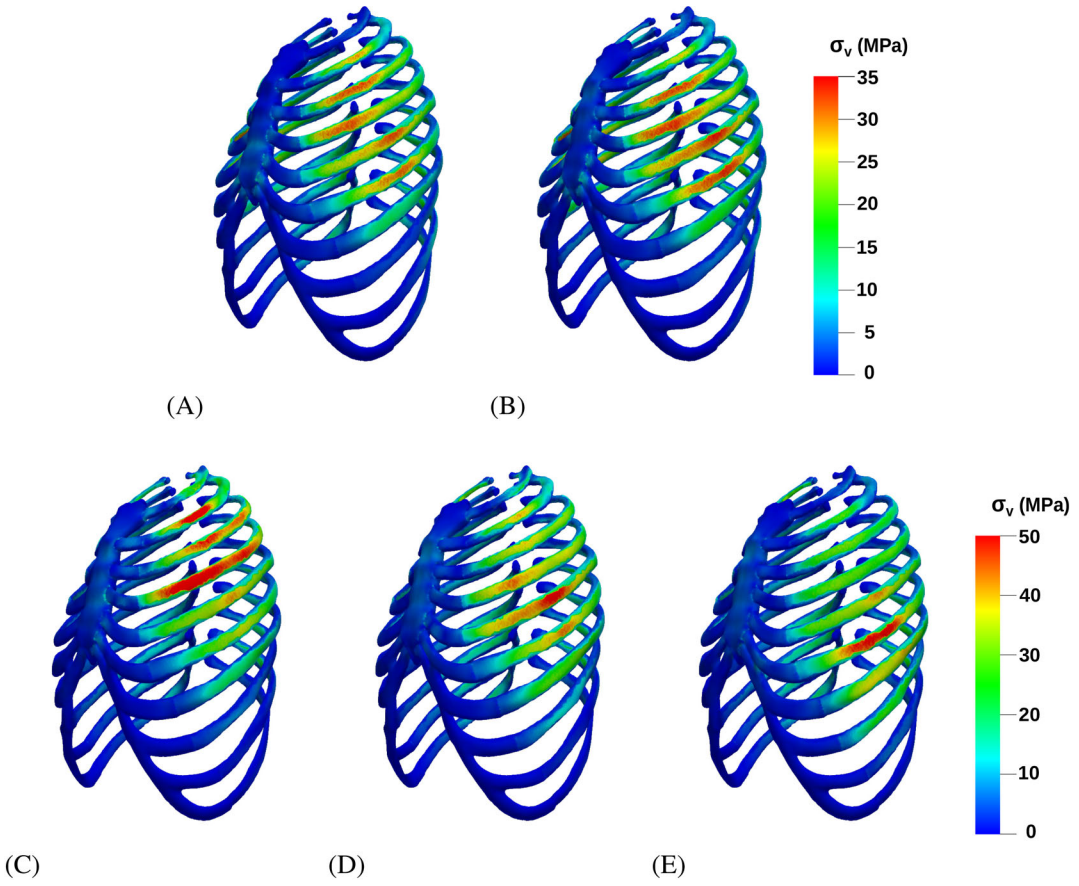

FIGURE 7 Von Mises stress distributions (σ_v) on the rib cage when a 600 N force was applied at the compression region: (A) P1, (B) P2, (C) P3, (D) P4, and (E) P5. For the sake of clarity a different color scale range was used for P1 and P2

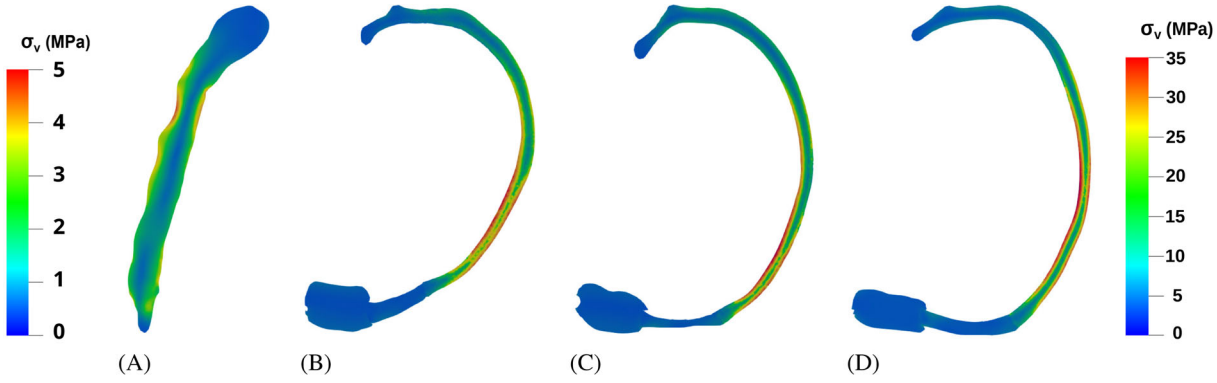

FIGURE 8 Von Mises stress distributions (σ_v) on selected slices for the case with a 600 N force applied at the compression region P2. In part (A), the slice corresponds to the saggital mid-plane along the breastbone, with the σ_v levels as shown in the leftmost colorbox. In parts (B–D), slices along the breastbone, costal cartilages and osseous ribs are respectively shown for the 3rd, 4th, and 5th left ribs, with the σ_v levels in the rightmost colorbox

interesting to compare the performance of the two locations on the breastbone, P1 and P2. Even though both compression regions meet the localization requirement set by the CPR guidelines it turns out that P2, which is caudally shifted from P1 a 16% of the total length of the breastbone (see Figure 1), is more efficient in terms of the force needed to achieve a given compression depth. Let us consider, for example, the force $F_{5\text{cm}}$ required to achieve a compression depth of $\Delta h = 5$ cm. The 16% caudal shift from P1 to P2 results in a 11% (17%) reduction in $F_{5\text{cm}}$ on the breastbone P1

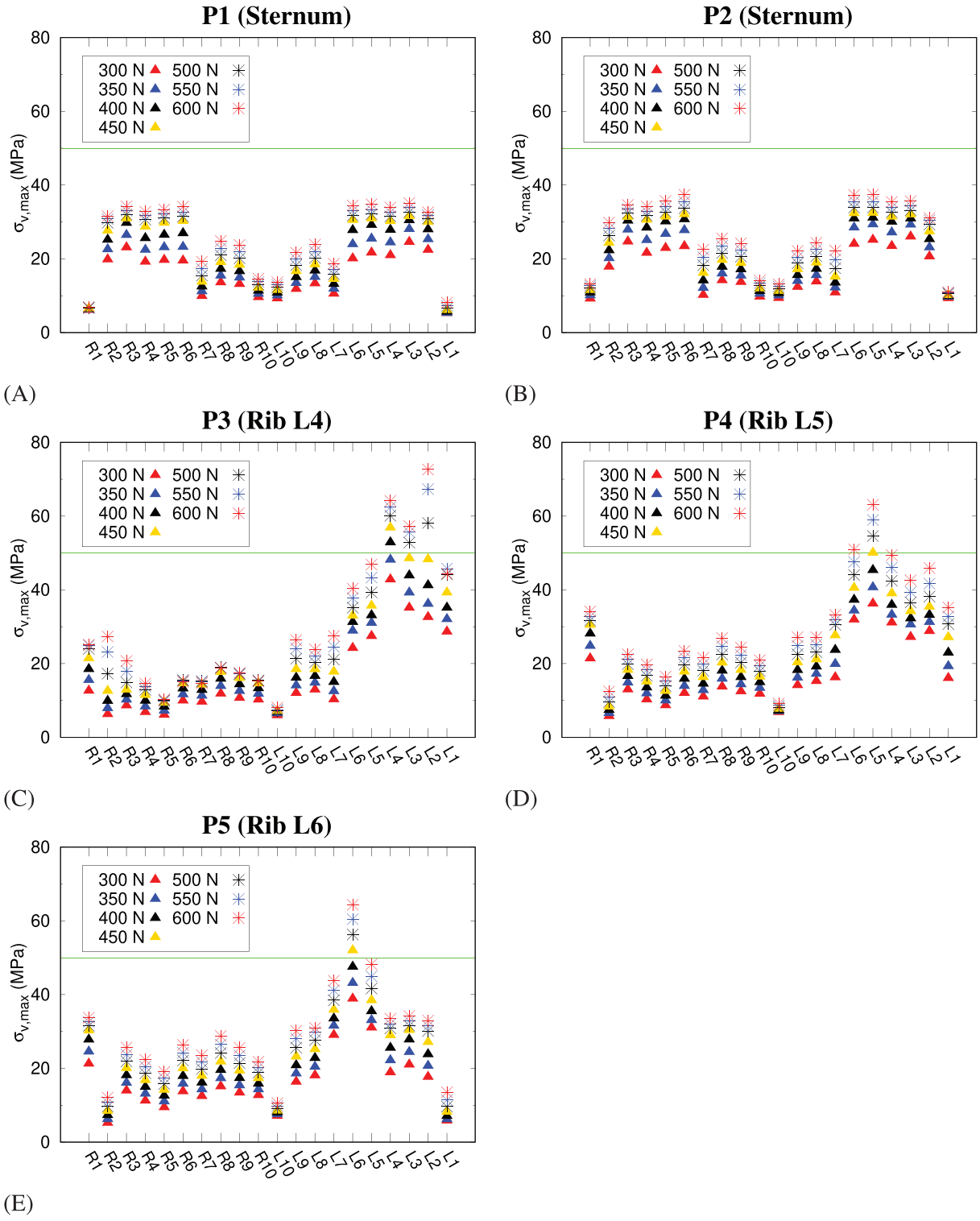

FIGURE 9 Maximum value of the von Mises tension on each of the ribs when a force ranged between 200 N and 600 N in increments of 50 N was applied at the five compression locations: (A) P1, (B) P2, (C) P3, (D) P4, and (E) P5. Right (left) ribs are denoted as R (L) followed by their number

(P2) area and about 12% in the P4 and P5 areas. Figure 6C shows that the P2 compression region remains more efficient than P1 on the P3 area even though the target compression depth of $\Delta h = 5$ cm on the P3 area is not reached.

The results in Figure 6 show that the P3 region, placed on the 4th left costal cartilage, presents two different behaviors. For forces below 400 N it turns out to be the least efficient in terms of compression depth, in all the regions except

in the fourth left rib. For higher forces, the depth achieved using the P3 compression region increases rapidly with increasing F at the cost of large deformations of the 1th and 4th left ribs, as shown in Figure 4D for $F = 600$ N.

If we compare the performance of the P2 and P4 compression regions, we see that the use of the latter region leads to a 21% F_{5cm} increase in the P2 breastbone area (Figure 6B) and to F_{5cm} decreases of 18% and 20% in the P4 and P5 areas, respectively (Figure 6D,E). In addition, the use of P4 makes it possible to reach the target compression depth of $\Delta h = 5$ cm in the P3 area with $F < 600$ N (Figure 6B). Comparison of the P2 and P5 compression regions gives an increase in F_{5cm} of 28% and 5% in the P2 and P4 areas, respectively (Figure 6B,D) and a decrease in F_{5cm} of 30% in the P5 area (Figure 6E).

A key factor to evaluate the merits of the different compression regions is the associated risk of an injury, which in the current study is assessed using the von Mises tension, σ_v. The σ_v distributions on the rib cage for the simulations with $F = 600$ N are shown in Figure 7, where the rib cage elements that are under higher stresses can be clearly identified. The highest σ_v values are mostly attained at the lateral region of the ribs, consistently with the results of the single rib simulation plotted in Figure 3B. Figure 8 shows the σ_v distributions on selected cross-sections of the breastbone and the 3rd, 4th and 5th left ribs for the case with a force of $F = 600$ N applied in the P2 area. Note that Figure 8B–D is consistent with the plots in Figure 7, in the sense that the σ_v peaks in the osseous part of the ribs are located near the rib surface, whereas the stress levels supported by the costal cartilages are comparatively modest. Also, Figure 8A shows that the σ_v peak values within the breastbone are, at most, as high as 5 MPa, that is, almost an order of magnitude lower than they are in the osseous ribs. Note also that even though in this simulation pressure is applied at the P2 region, which is located not far from xiphoid process (see Figure 1C), the maximum stress levels in Figure 8A are found in the upper breastbone, that is, closer to the manubrium.

When the compression is performed on P3, P4, or P5, the $\sigma_v = 50$ MPa reference value is exceeded on different ribs (see Figure 7C–E). It is remarkable that the maximum σ_v values in these plots are roughly the same as those plotted in Figure 3B for a single rib bending simulation considering that the compression force applied to the P3, P4, and P5 locations is much larger ($F = 600$ N instead of 60 N). Kindig et al.[50] described a similar phenomenon as load sharing in their measurements on cadaveric rib cages when unilateral loads were applied to a particular rib. These authors reported that as the ribs are connected to the sternum the latter element transfers a good deal of the load applied to one rib into the surrounding ribs above and below.

Figure 9 shows the maximum tension $\sigma_{v,max}$ supported by each of the ribs as a function of F. For the compression regions located on the breastbone (P1 and P2, see Figure 9A,B) the highest $\sigma_{v,max}$ values on the ribs, always under 40 MPa, are reached on the 2nd to 6th ribs. When compression force is applied on the 4th left costal cartilage (P3, Figure 9C), the highest $\sigma_{v,max}$ is reached on the fourth left rib for forces below 450 N and on the 2nd left rib for higher forces, reaching a value as high as $\sigma_{v,max} = 73$ MPa for $F = 600$ N. For the compression regions P4 and P5, Figure 9D,E shows that $\sigma_{v,max}$ is always found on the rib associated to the costal cartilage where they are located. In these ribs (L5 and L6), considerably high values of $\sigma_{v,max}$ are reached even at a force as low as $F = 300$ N and high values above $\sigma_{v,max} = 50$ MPa are achieved for forces above $F = 450$ N. The two ribs next to the rib where compression is performed, namely the 4th and 6th left ribs in the P4 case and the 5th and 7th left ribs in the P5 case, achieve also significantly high $\sigma_{v,max}$ values (Figures 7 and 9D,E).

4 | DISCUSSION AND CONCLUSIONS

Current numerical simulations are consistent with previously reported observations during chest compression maneuvers. In particular, the V–shaped deformed geometries shown in Figure 5 are in a good qualitative agreement with previously reported CT images (see Figure 5 in Rutty et al.[52]). The relationship between compression depth and force plotted in Figure 6 reveals that the stiffness of the rib cage tends to increase with increasing compression force. Such a mechanical behavior is qualitatively consistent with the experimental results reported by Tomlinson et al.[53] Note that the force–depth behaviors plotted in Figure 6 seem to contradict those displayed in Figure 3 for the compression of individuals ribs. That is, standalone ribs when compressed tend to become increasingly softer whereas the whole rib cage tends to become increasingly stiffer with increasing applied force. The effect of the ICM linking adjacent ribs might provide an explanation for such a contradiction. However, in additional simulations performed without the ICM we found that the progressive hardening of the rib cage persisted. An alternative explanation for this phenomenon is in the relatively strong initial bending of costal cartilages at low-compression forces. Once cartilages have achieved their maximum angulation a further compression of the chest requires a progressive bending of the osseous part of the ribs.

As the osseous tissue is markedly more rigid than the cartilaginous one, a considerably larger increase in force is required to bend the ribs.

Our results also show that a caudal displacement of the compression location along the breastbone toward its lower tip, that is, from P1 to P2, results in a higher compression depth on both locations. This is also a somewhat unexpected fact that needs a further discussion. Chest CT scans indicate that the breastbone moves predominantly at the bottom end during CPR maneuvers,[14] a biomechanical behavior that is also predicted by our simulations, as illustrated in Figure 10. Pickard et al.[14] explained the biomechanics observed for the breastbone through the so–called hinge mechanism, which suggests that the breastbone is, basically, superiorly fixed. These authors noted that such a superior fixation is actually inherent to CPR maneuvers as a 4–5 cm posterior displacement of the whole breastbone would most probably cause the occlusion of the trachea and major arteries, a situation which is not seen in clinical practice. The effects of the hinge mechanism was also markedly visible in the measurements reported by Kinding et al.[50] for compression forces of about $F = 100$ N applied into the lower sternum (see Figure 23 in their paper). Present results provide an explanation for the hinge mechanism in terms of rib cage mechanics, as discussed in what follows. If we associate the breastbone compression depth with its revolved angle around the hinge axis in Figure 10, we see that the difference in performance between the P1 and P2 compression regions is already observed when the lowest force of $F = 200$ N is applied. When the force is further increased to 400 and 600 N, the resulting increase in the revolved angle is roughly the same for both P1 and P2. As discussed above, application of the compression force on the breastbone produces the early bending of the costal cartilages. Let us now focus on the three pair of ribs closer to the compression location, namely 3rd to 5th ribs for P1 and 4th to 6th ribs for P2 (see Figure 1). In terms of most affected ribs, moving the compression location from P1 to P2 implies swapping the 3rd and 6th pairs of ribs. The cartilages in the upper ribs are considerably shorter than are the ones in the lower ribs (see Figure 1) and so is the breastbone compression depth required to attain the maximum angulation of the cartilage. Once the cartilage has reached its maximum angulation, a second stage begins in which it is the osseous part of the rib, which poses a higher resistance to bending. The shorter compression depths achieved when P1 is used instead of P2 would therefore be a consequence of an earlier transition in the upper ribs between the cartilage angulation stage and the osseous rib bending stage.

Another interesting question is to what extent the maximum stress values ($\sigma_{v,max}$), plotted in Figure 9, are indicative, at a qualitative level, of the real risk of injury during chest compressions. A distribution of the percentage of rib fractures and sternocostal separations during CPR performed on the breastbone was reported by Krajl et al.[19] These authors analyzed a sample of 1480 male patients and found that 1268 of them sustained one or more skeletal chest injuries. They identified rib fractures in 77% of males and 85% of females and sternocostal separations in 33% of males and 12% of females. Ribs with highest percentage of fractures were 2nd to 6th ribs (see Figure 3 in Krajl et al.[19]), which are precisely those with highest $\sigma_{v,max}$ values in Figure 9A,B.

In regard of the merits of each of the five compression locations considered in this study, comparison of the P1 and P2 compression regions on the breastbone strongly suggests that the latter would be preferable. In more practical terms, we have seen that while both P1 and P2 would produce similar maximum tensions in the ribs (Figure 9) the force

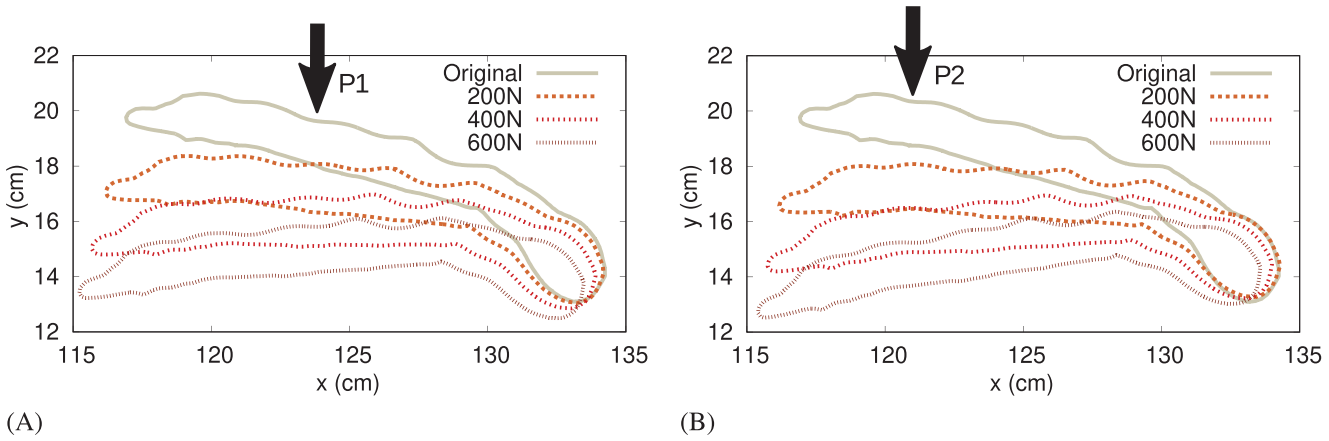

FIGURE 10 Variation with force of the contour of the breastbone at the frontal plane that divides it into two halves for the two compression regions located on the breastbone: (A) P1, (B) P2. The original breastbone (no compression force applied) and the displaced breastbone for three different values of the compression force, namely $F = 200$, 400, and 600 N, are included in both plots

required to reach the target compression depth of $\Delta h = 5$ cm on the breastbone P1 (P2) area is 11% (17%) lower when using P2 (see Figure 6A,B). In other words, caudally shifting the compression location a 16% of the total length of the breastbone toward its inferior tip would result in a more effective CPR in terms of the compression depth achieved on the lower part of the breastbone and on the cartilages of the 4th, 5th, and 6th left ribs, that is, in the region of interest where the left ventricle is most commonly placed.[11,17]

A comparative analysis of the maximum displacements plotted in Figure 6 indicates that P3 is the one with the poorest performance in terms of the achieved compression depth and potential risk of injuries. The use of this location would require a force of about 550 N to achieve the recommended compression depth of $\Delta h = 5$ cm on the breastbone (Figure 6A,B). Application of such a large force on the P3 area might well imply a high risk of fracture of the 4th and 2nd left ribs (see Figure 9C), and costo–sternal separation of the 1th left rib (see Figure 4D).

Both compression regions P4 and P5 achieve fairly high-compression depths in the breastbone (Figure 6A,B). In terms of compression depth achieved in the 4th to 6th left ribs, it is more efficient to apply the compression force on P4 rather than on P5. In any case, the application of high forces ($F \geq 500$ N) over these two regions might again be problematic because of the large displacements, as high as 7 and 8 cm in the 5th and 6th left rib, respectively (see Figure 6D,E), along with the high-maximum tension values ($\sigma_v > 50$ MPa) on these ribs (Figure 9D,E).

The use of the P4 compression region provides the target depth on the 4th–6th left costal cartilages, beneath which the left ventricle will probably be located, at comparatively modest levels of the applied force. Thus, P4 might be a good candidate as an alternative location for CPR maneuvers, especially under operating conditions when the use of high-compression forces would be precluded. On the contrary, the results of the present study suggest that P3 and P5 would not be good candidates for CPR compression locations. The P5 compression region is just less efficient than P4 in terms of achieved compression depth while adding no other benefit. The P3 region should be, according to our simulations, avoided as a CPR compression location because of both its lesser efficiency and the high risk of injuries even at relatively low-compression forces.

We note that in view of the limitations of the current study, discussed below, our considerations on the relative merits of the different CPR compression locations are by no means conclusive but merely prospective. Further numerical and experimental research would be needed to assess the levels of safety and hemodynamic efficiency associated with the use of alternative compression locations in CPR maneuvers.

4.1 | Study limitations

The current study has several limitations. One limitation is that the chest model used in the simulations does not include skin, subcutaneous fat or intrathoracic fat and organs. Nevertheless, the hysterical damping caused by internal frictions of these intrathoracic structures has been partially taken into account in the current simulations by assuming characteristic parameters for bone and ICM that resulted in a bias toward a relatively stiff rib cage model.

A second limitation is in the fact that the subject being modeled in the current study is a young male with a normal body mass index, but the most common recipients of CPR tend to be old and obese individuals. Holcombe et al.[54] studied the effect of age, height, weight, and sex on the rib cage aspect ratio. These authors measured the geometry of 20,627 ribs from CT scans of 1042 adult subjects and found that sex and height had negligible influence on the aspect ratio and that weight alone was the variable that better predicted rib angles. They concluded that obesity was strongly related to a lower aspect ratio of the rib cage, which means that ribs tend to adopt a more horizontal configuration (barrel–chested) in obese individuals. On the other hand, they found that rib cage aspect ratio increased (narrow–chested) with age.

It is important to note that the bone tissue is in fact orthotropic but high-resolution images that capture the microstructures of the tissue are required in order to model the detailed mechanical behavior. If micro-CT images of the ribcage osseous elements were available for future research then it would be possible to systematically determine the map of their anisotropic directions[44–46] (see Reference 46, for examples of application of such methodology to femoral and mandibular bone tissue). Moreover, in the present study the osseous rib was modeled as a single material when in fact it is composed of cortical and trabecular bone. In this respect, it is interesting to note that Arregui et al.[55] reported that in their FE simulations of clavicle compression the presence of trabecular bone in their model did not significantly affect any of the structural or failure mechanics. The authors attributed this lack of significance of trabecular bone to the fact that the predominant loading mode was bending, a condition, which is also present in our simulations with the bending of the ribs during chest compression. Nevertheless, we assessed that the present homogeneous model for the osseous rib yielded a response to quasistatic frontal loading that was within the expected experimental range (Figure 3).

In the present model, costal cartilages are rigidly connected to the breastbone. That is, the sternochondral joints are not included in the model. In this particular, we have followed the common trend from previous FE studies of ribcage mechanics.[25,27,39,56] It is noteworthy that even in previous FE ribcage simulations where either the costovertebral[25] or the sternoclavicular[56] joints were carefully modeled, the sternochondral joints were omitted. It seems reasonable to assume that, as thoroughly discussed in Section 2, ribcage compression is, on the overall, well predicted with rigid models (no sternochondral joints). However, in the present study the absence of sternochondral joints excludes a proper assessment of the risk of separation of the costal cartilage from the breastbone during the CPR maneuvers.[19]

The scope of the present study is somewhat limited by the use of a single geometry model. FE models offer the possibility to apply different conditions to a unique geometry, an option not available in measurements in a real patient as CPR would be performed using only one compression location. The use of cadavers would be of little help as usually several ribs break during CPR. The question is to what extent FE results obtained for a particular subject can be extended to the general population considering the huge inter-subject variation both in rib cage morphology[54,57–59] and in the mechanical properties of the different tissues involved. A possible strategy to assess the variations of rib cage mechanics with body mass index, stature, age, and gender is the morphing of an existing FE geometry model.[27,60,61] Iraeus et al.[28] explored the introduction of human variability in the commonly used rib fracture prediction FE methodologies[62–64] in the context of automobile safety research. Iraeus et al.[28] recommended, as an initial step toward their global goal, that the rib cross-sectional height be accurately modeled in future FE studies. In the present work, we opted for a simpler approach by analyzing and discussing our results mainly at a qualitative level. We focused on the comparison between the different CPR compression locations and on the mechanics involved in rib cage compression. In particular, the present results are in good qualitative agreement with previously reported observations during chest compression maneuvers, such as the V-shaping of the rib cage (Figure 5), the pseudo hyper-elastic behavior (increasing stiffness) of skeletal chest (Figure 6), and the so-called hinge mechanism (Figure 10).

ACKNOWLEDGEMENT

This work was supported by Universitat Rovira i Virgili under Grant 2018PFR-URV-B2-29.

CONFLICT OF INTEREST

No potential conflict of interest was reported by the authors.

DATA AVAILABILITY STATEMENT

Research data are not shared.

ORCID

Josep M. López https://orcid.org/0000-0001-7541-8936

REFERENCES

1. Gräsner JT, Lefering R, Koster RW, et al. EuReCa ONE–27 nations, ONE Europe, ONE registry. A prospective one month analysis of out–of–hospital cardiac arrest outcomes in 27 countries in Europe. *Resuscitation*. 2016;105(8):188-195.
2. Andersen LW, Holmberg MJ, Berg KM, Donnino MW, Granfeldt A. In–hospital cardiac arrest. A review. *JAMA*. 2019;321(12):1200-1210.
3. Hasselqvist-Ax I, Riva G, Herlitz J, et al. Early cardiopulmonary resuscitation in out-of-hospital cardiac arrest. *New England J Med*. 2015;372(24):2307-2315. doi:10.1056/NEJMoa1405796
4. Kouwenhoven WB, Jude JR, Knickerbocker GG. Closed-chest cardiac massage. *JAMA*. 1960;173(10):1064-1067.
5. Stiell I, Brown S, Nichol G, et al. What is the optimal chest compression depth during out–of–hospital cardiac arrest resuscitation of adult patients? *Circulation*. 2014;130(22):1962-1970.
6. Perkins G, Handley A, Koster R, et al. European resuscitation council guidelines for resuscitation 2015. Section 2. Adult basic life support and automated external defibrillation. *Resuscitation*. 2015;95:81-99.
7. Qvigstad E, Kramer-Johansen J, Tømte T, et al. Clinical pilot study of different hand positions during manual chest compressions monitored with capnography. *Resuscitation*. 2013;84(9):1203-1207.
8. Skulec R, Vojtisek P, Cerny V. Correlation between end–tidal carbon dioxide and the degree of compression of heart cavities measured by transthoracic echocardiography during cardiopulmonary resuscitation for out–of–hospital cardiac arrest. *Crit Care*. 2019;23:334.
9. Chalkias A, Arnaoutoglou E, Xanthos T. Personalized physiology-guided resuscitation in highly monitored patients with cardiac arrest—the PERSEUS resuscitation protocol. *Heart Fail Rev*. 2019;24(4):473-480.
10. Hwang S, Lee K, Cho J, Yoon J, Choe K. Changes of aortic dimensions as evidence of cardiac pump mechanism during cardiopulmonary resuscitation in humans. *Resuscitation*. 2001;50(1):87-93.

11. Papadimitriou P, Chalkias A, Mastrokostopoulos A, Kapniari I, Xanthos T. Anatomical structures underneath the sternum in healthy adults and implications for chest compressions. *Am J Emerg Med*. 2013;31(3):549-555.
12. Hwang SO, Zhao PG, Choi HJ, et al. Compression of the left ventricular outflow tract during cardiopulmonary resuscitation. *Acad Emerg Med*. 2009;16(10):928-933. doi:10.1111/j.1553-2712.2009.00497.x
13. Catena E, Ottolina D, Fossali T, et al. Association between left ventricular outflow tract opening and successful resuscitation after cardiac arrest. *Resuscitation*. 2019;138:8-14.
14. Pickard A, Darby M, Soar J. Radiological assessment of the adult chest: implications for chest compressions. *Resuscitation*. 2006;71(3): 387-390. doi:10.1016/j.resuscitation.2006.04.012
15. Shin J, Rhee JE, Kim K. Is the inter-nipple line the correct hand position for effective chest compression in adult cardiopulmonary resuscitation? *Resuscitation*. 2007;75:305-310. doi:10.1016/j.resuscitation.2007.05.003
16. Cha K, Kim Y, Shin H, et al. Optimal position for external chest compression during cardiopulmonary resuscitation: an analysis based on chest CT in patients resuscitated from cardiac arrest. *Emerg Med J*. 2013;30(8):615-619.
17. Nestaas S, Stensaeth K, Rosseland V, Kramer-Johansen J. Radiological assessment of chest compression point and achievable compression depth in cardiac patients. *Scand J Trauma Resusc Emerg Med*. 2016;24:54.
18. Anderson K, Castaneda M, Boudreau S, Sharon D, Bebarta V. Left ventricular compressions improve hemodynamics in a swine model of out–of–hospital cardiac arrest. *Prehosp Emerg Care*. 2017;21(2):272-280.
19. Kralj E, Podbregar M, Kejžar N, Balažic J. Frequency and number of resuscitation related rib and sternum fractures are higher than generally considered. *Resuscitation*. 2015;93:136-141.
20. Miller AC, Rosati SF, Suffredini DS. A systematic review and pooled analysis of CPR–associated cardiovascular and thoracic injuries. *Resuscitation*. 2014;85(6):724-761.
21. Ihnát Rudinská L, Hejna P, Ihnát P, Tomášková H, Smatanová M, Dvořáček I. Intra–thoracic injuries associated with cardiopulmonary resuscitation – frequent and serious. *Resuscitation*. 2016;103(6):66-70.
22. Azeli Y, Barbería E, Jiménez-Herrera M, Amejilde A, Bardají A. Serious injuries secondary to cardiopulmonary resuscitation: incidence and associated factors (Incidencia y variables asociadas a lesiones graves secundarias a reanimación cardiopulmonar). *Emerg: Revista de la Soc Espanola de Med de Emerg*. 2019;31(5):327-334.
23. Azeli Y, Lorente Olazabal J, Monge García M, Bardají A. Understanding the adverse hemodynamic effects of serious thoracic injuries during cardiopulmonary resuscitation: a review and approach based on the Campbell diagram. *Front Physiol*. 2019;10:1-6.
24. Charbonney E, Delisle S, Savary D, et al. A new physiological model for studying the effect of chest compression and ventilation during cardiopulmonary resuscitation: the Thiel cadaver. *Resuscitation*. 2018;125:135-142.
25. Kindig M, Li Z, Kent R, Subit D. Effect of intercostal muscle and costovertebral joint material properties on human ribcage stiffness and kinematics. *Comput Methods Biomech Biomed Eng*. 2015;18(5):556-570. doi:10.1080/10255842.2013.820718
26. Poulard D, Kent RW, Kindig M, Li Z, Subit D. Thoracic response targets for a computational model: a hierarchical approach to assess the biofidelity of a 50th-percentile occupant male finite element model. *J Mech Behav Biomed Mater*. 2015;45:45-64. doi:10.1016/j.jmbbm.2015.01.017
27. Schoell SL, Weaver AA, Vavalle NA, Stitzel JD. Age– and sex–specific thorax finite element model development and simulation. *Traffic Inj Prev*. 2015;16(suppl 1):557-565. doi:10.1080/15389588.2015.1005208
28. Iraeus J, Brolin K, Pipkorn B. Generic finite element models of human ribs, developed and validated for stiffness and strain prediction – to be used in rib fracture risk evaluation for the human population in vehicle crashes. *J Mech Behav Biomed Mater*. 2020;106:103742. doi:10.1016/j.jmbbm.2020.103742
29. Hellevuo H, Sainio M, Nevalainen R, et al. Deeper chest compression – more complications for cardiac arrest patients? *Resuscitation*. 2013;84(6):760-765.
30. Mitsuhashi N, Fujieda K, Tamura T, Kawamoto S, Takagi T, Okubo K. BodyParts3D: 3D structure database for anatomical concepts. *Nucleic Acids Res*. 2009;37(suppl 1):D782-D785. doi:10.1093/nar/gkn613
31. Nagaoka T, Watanabe S, Sakurai K, et al. Development of realistic high-resolution whole-body voxel models of Japanese adult males and females of average height and weight, and application of models to radio–frequency electromagnetic–field dosimetry. *Phys Med Biol*. 2004;49(1):1-15. doi:10.1088/0031-9155/49/1/001
32. Geuzaine C, Remacle JF. Gmsh. A three-dimensional finite element mesh generator with built-in pre- and post-processing facilities. http://gmsh.info/; 2020.
33. Code Aster . Structures and thermomechanics analysis for studies and research. https://www.code-aster.org/spip.php?rubrique2, 2020.
34. Baubin M, Kollmitzer J, Pomaroli A, et al. Force distribution across the heel of the hand during simulated manual chest compression. *Resuscitation*. 1997;35(3):259-263.
35. McCormick WF. Mineralization of the costal cartilages as an indicator of age: preliminary observations. *J Forensic Sci*. 1980;25(4):736-741.
36. Lau A, Oyen ML, Kent RW, Murakami D, Torigaki T. Indentation stiffness of aging human costal cartilage. *Acta Biomater*. 2008;4:97-103. doi:10.1016/j.actbio.2007.06.008
37. Forman JL. The structural characteristics of the costal cartilage: the roles of calcification and the perichondrium, and the representation of the costal cartilage in finite element models of the human body. Cambridge: Ph.D. Dissertation. University of Virginia School of Engineering and Applied Science, Department of Mechanical and Aerospace Engineering. 2009.
38. Lau A, Kindig M, Salzar R, Kent R. Micromechanical modeling of calcifying human costal cartilage using the generalized method of cells. *Acta Biomater*. 2015;18:226-235.

39. Forman JL, Kent RW. The effect of calcification on the structural mechanics of the costal cartilage. *Comput Methods Biomech Biomed Eng*. 2014;17(2):94-107. doi:10.1080/10255842.2012.671307
40. Forman J, Kent R. Modeling costal cartilage using local material properties with consideration for gross heterogeneities. *J Biomech*. 2011;44(5):910-916.
41. Forman JL, del Pozo de Dios E, Arregui-Dalmases C, Kent RW. The contribution of the perichondrium to the structural mechanical behavior of the costal–cartilage. *ASME J Biomech Eng*. 2010;132(094501):94501–1-94501–5.
42. Mitton D, Minonzio JG, Talmant M, et al. Non-destructive assessment of human ribs mechanical properties using quantitative ultrasound. *J Biomech*. 2014;47(6):1548-1553.
43. Katzenberger MJ, Albert DL, Agnew AM, Kemper AR. Effects of sex, age, and two loading rates on the tensile material properties of human rib cortical bone. *J Mech Behav Biomed Mater*. 2020;102(103410):21. doi:10.1016/j.jmbbm.2019.103410
44. Yi W, Heo M, Lee S, Choi S, Huh K, Lee S. Direct measurement of trabecular bone anisotropy using directional fractal dimension and principal axes of inertia. *Oral Maxillofac Radiol*. 2007;104(1):110-116. doi:10.1016/j.tripleo.2006.11.005
45. Maggiano IS, Maggiano CM, Clement JG, Thomas CDL, Carter Y, Cooper DML. Three–dimensional reconstruction of Haversian systems in human cortical bone using synchrotron radiation–based micro–CT: morphology and quantification of branching and transverse connections across age. *J Anat*. 2016;228:719-732. doi:10.1111/joa.12430
46. Toniolo I, Salmaso C, Bruno G, et al. Anisotropic computational modelling of bony structures from CT data: an almost automatic procedure. *Comput Methods Programs Biomed*. 2020;189(105319):1-11. doi:10.1016/j.cmpb.2020.105319
47. Baier W, Norman DG, Williams MA. Micro–CT for the examination of paediatric rib injuries: a case series. *Forensic Sci Int*. 2021;325(110789):1-6. doi:10.1016/j.forsciint.2021.110789
48. Kindig M, Lau AG, Kent RW. Biomechanical response of ribs under quasistatic frontal loading. *Traffic Inj Prev*. 2011;12(4):377-387. doi:10.1080/15389588.2011.583960
49. Kent R. Frontal thoracic response to dynamic loading: the role of superficial tissues, viscera and the rib cage. *Int J Crashworthiness*. 2008;13(3):289-300. doi:10.1080/13588260801933725
50. Kindig MW, Lau AG, Forman JL, Kent RW. Structural response of cadaveric ribcages under a localized loading: stiffness and kinematic trends. *Stapp Car Crash J*. 2010;54:10S-19S.
51. Beesems SG, Hardig BM, Nilsson A, Koster RW. Force and depth of mechanical chest compressions and their relation to chest height and gender in an out-of-hospital setting. *Resuscitation*. 2015;91:67-72.
52. Rutty GN, Robinson C, Amoroso J, Coats T, Morgan B. Could post-mortem computed tomography angiography inform cardiopulmonary resuscitation research? *Resuscitation*. 2017;121:34-40. doi:10.1016/j.resuscitation.2017.09.022
53. Tomlinson A, Nysaether J, Kramer-Johansen J, Steen P, Dorph E. Compression force–depth relationship during out-of-hospital cardiopulmonary resuscitation. *Resuscitation*. 2007;72:364-370. doi:10.1016/j.resuscitation.2006.07.017
54. Holcombe SA, Wang SC, Grotberg JB. The effect of age and demographics on rib shape. *J Anat*. 2017;231:229-247. doi:10.1111/joa.12632
55. Arregui-Dalmases C, Pozo DE, Duprey S, et al. A parametric study of hard tissue injury prediction using finite elements: consideration of geometric complexity, subfailure material properties, CT–thresholding, and element characteristics. *Traffic Inj Prev*. 2010;11:286-293. doi:10.1080/15389581003709902
56. Lim BY, Kim Y, Hoseok I, Lee CS. Numerical investigation of the sternoclavicular joint modeling technique for improving the surgical treatment of pectus excavatum. *Sci Rep*. 2020;10(7357):7357. doi:10.1038/s41598-020-64482-7
57. Shi X, Cao L, Reed M, Rupp J, Hoff C, Hu J. A statistical human rib cage geometry model accounting for variations by age, sex, stature and body mass index. *J Biomech*. 2014;47(10):2277-2285. doi:10.1016/j.jbiomech.2014.04.045
58. Weaver A, Schoell S, Stitzel J. Morphometric analysis of variation in the ribs with age and sex. *J Anat*. 2014;225(2):246-261. doi:10.1111/joa.12203
59. Wang Y, Cao L, Bai Z, et al. A parametric ribcage geometry model accounting for variations among the adult population. *J Biomech*. 2016;49(13):2791-2798. doi:10.1016/j.jbiomech.2016.06.020
60. Hu J, Zhang K, Fanta A, et al. Stature and body shape effects on driver injury risks in frontal crashes: a parametric human Modelling study. *IRCOBI Conference*; September 2017;IRC–17–85:656–667.
61. Zhang K, Cao L, Fanta A, et al. An automated method to morph finite element whole–body human models with a wide range of stature and body shape for both men and women. *J Biomech*. 2017;60:253-260. doi:10.1016/j.jbiomech.2017.06.015
62. Trosseille X, Baudrit P, Leport T, Vallancien G. Rib cage strain pattern as a function of chest loading configuration. *Stapp Car Crash J*. 2008;52:205-231.
63. Li Z, Kindig MW, Kerrigan JR, et al. Rib fractures under anterior—posterior dynamic loads: experimental and finite–element study. *J Biomech*. 2010;43:228-234. doi:10.1016/j.jbiomech.2009.08.040
64. Forman JL, Kent RW, Mroz K, Pipkorn B, Bostrom O, Segui-Gomez M. Predicting rib fracture risk with whole–body finite element models: development and preliminary evaluation of a probabilistic analytical framework. *Ann Adv Automot Med*. 2012;56:109-124.

How to cite this article: Suazo M, Herrero J, Fortuny G, Puigjaner D, López JM. Biomechanical response of human rib cage to cardiopulmonary resuscitation maneuvers: Effects of the compression location. *Int J Numer Meth Biomed Engng*. 2022;38(4):e3585. doi:10.1002/cnm.3585